

Room temperature fabrication of silicon nanocrystals by pulsed laser deposition

Erika Biserni · Alice Scarpellini ·
Rosaria Brescia · David Dellasega ·
Andrea Li Bassi · Paola Bruno

Received: 4 September 2013 / Accepted: 14 May 2014

E. Biserni (✉) · A. Li Bassi · P. Bruno
Center for Nano Science and Technology @PoliMi,
Istituto Italiano di Tecnologia, Via Pascoli 70/3,
20133 Milan, Italy
e-mail: erika.biserni@iit.it

E. Biserni · D. Dellasega · A. Li Bassi
Dipartimento di Energia, Politecnico di Milano, Via
Ponzio 34, 20133 Milan, Italy

A. Scarpellini · R. Brescia
Department of Nanochemistry, Istituto Italiano di
Tecnologia, Via Morego 30, 16163 Genoa, Italy

Introduction

In the last years, a renewed and increasing interest toward the optoelectronic properties of silicon nanocrystals (Si NCs) and nanostructures has been registered as far as concerns their fabrication, characterization, and possible implementation in devices, such as high efficiency solar cells (Conibeer 2010), Si NC non-volatile memories (Muralidhar et al. 2009), biomedical devices and sensors (Borsella et al. 2010), lithium batteries (Kim et al. 2010), and thermoelectric devices (Suzuki et al. 2012).

Wide knowledge on the bulk properties of silicon and related technologies is well consolidated; its properties at the nanoscale, however, have been only partially explored and, although 3rd generation photovoltaics is one of the most targeted applications for silicon nanocrystals (Tsakalagos 2008; Conibeer et al. 2010; König et al. 2010; Nozik 2002; Luque et al. 2007), no QD-based solar devices showing enhanced

efficiency due to quantum confinement effects have been yet presented to the best of our knowledge. At the state of the art, the synthesis of silicon QDs in view of photovoltaic applications has been achieved mainly by the Plasma-Enhanced Chemical Vapour Deposition (PECVD) technique (Hartel et al. 2011; Park et al. 2008; Conibeer et al. 2006) or through chemical ways by means of precipitation from colloidal solutions (Cheng et al. 2012). Recent works have been published on fabrication and characterization of silicon QDs (Hartel et al. 2011), where the “superlattice approach” is explored. The idea of the superlattice consists of depositing via silane-assisted PECVD a stack of alternated layers of Si-rich and stoichiometric dielectric material (SiO_x , SiC , SiN_x) and let Si QDs precipitate at the interfaces upon high-temperature annealing. Sputtering has been used in a similar approach also by Conibeer, Green, and Park to fabricate silicon QDs (Park et al. 2008; Conibeer et al. 2006). However, the seeking for a process that avoids harmful materials, such as silane, and does not involve high temperature steps would be relevant especially for future developments in the field of hybrid photovoltaics (organic–inorganic solar cells) or flexible devices deposited on plastic (polymeric) substrates. At present, though, effective strategies for low temperature synthesis of Si QDs by physical methods are still scarce. In this direction, it is worth mentioning the work done by Kortshagen and his colleagues (Mangolini and Kortshagen 2007; Mangolini et al. 2005), who pioneered a low pressure process for the synthesis of Si nanocrystals in a radiofrequency-powered reactor. Despite the promising results of this work, headed for obtaining silicon nanocrystals from low pressure nonthermal plasma, it is important here to stress its major drawback related to the use of silane as a gas precursor.

It being a synthesis technique capable of working in out-of-equilibrium conditions, pulsed laser deposition (PLD) appears to be an interesting and promising pathway to achieve the goal of room- or low-temperature synthesis of Si QDs. Several examples of Si nanoparticle or nanostructured layers deposited by PLD in a background atmosphere are reported in the literature (Umezu et al. 2007, 2010; Cheng et al. 2010; Marine et al. 2000; Yuan 2010; Wu et al. 2008), starting from the work of Geohegan et al. (1998; Wood et al. 1998). However, direct evidence (e.g., high resolution TEM) of nanoparticle crystallinity is

usually lacking, unless high temperature post-deposition annealing procedures are adopted (Conibeer et al. 2009; König et al. 2010 and references therein). Most works focus on the investigation of photoluminescence (PL) properties, the interpretation of which is usually complicated by ex-situ oxidation, presence of defects, amorphous phase, and surface or interface states, and no clear conclusive evidence is reported of quantum confinement effects due the presence of nm-size crystalline quantum dots (e.g., in PL or Raman spectra).

In PLD, the background gas pressure is one of the parameters that most influence the structure and morphology of the deposited material (Dellasega et al. 2012; Fusi et al. 2009), by affecting the collision rate of ablated species within the plasma plume and thus enhancing cluster nucleation and growth and inducing a loss in kinetic energy of the deposited species. Low energy cluster deposition results in the growth of a porous layer, with porosity increasing as the pressure is increased (Casari and Bassi 2012; Merkulov et al. 1994). One of the main drawbacks in producing Si nanostructures is their being prone to oxidation (in situ and ex-situ), especially for the case of porous structures. Different strategies can be implemented in order to reduce oxidation, such as depositing an additive compact silicon layer on top of the film as a protective coating (Bruno et al. 2011).

Recently, Umezu et al. (Umezu et al. 2007; Umezu et al. 2010) have reported Si deposition by PLD in N_2 and H_2 background atmosphere and discussed the effect of surface passivation, as it is done for CVD synthesis of nano/microcrystalline thin films. However, in this case, Si nanoparticles are obtained at relatively high pressure (over 250 Pa, up to 1100 Pa), which induces foam-like structures instead of films. Moreover, structural characterization such as TEM analysis is not offering a conclusive proof of the crystalline nature of the nanostructures, and Raman spectra do not give evidence of confinement effects.

In this work, we show that films containing Si QDs with a size below 10 nm embedded in an amorphous matrix, together with unique silicon amorphous-crystalline core–shell (CS) nanostructures, can be fabricated at room temperature by PLD in an inert or very low (<3 vol%) H_2 -containing background processing atmosphere, at a pressure of 100 Pa. The use of H_2 is shown to reduce surface oxidation of the Si

nanostructures. The crystalline quality and the density of the Si QDs have been characterized by TEM and high resolution TEM, while Raman spectroscopy provides evidence of quantum confinement effects.

Experimental details

Nanocrystal-containing porous silicon films have been grown at room temperature by PLD. A KrF laser beam ($\lambda = 248$ nm, pulse energy 400 mJ, pulse duration 20 ns, repetition rate 20 Hz) was focused on a rotating and translating monocrystalline $\langle 100 \rangle$ silicon wafer target with a fluence of ~ 5 J/cm². After reaching a system base vacuum of approximately 3×10^{-3} Pa, a background gas was fluxed in the chamber during the whole deposition. In order to grow films of various morphologies, samples were produced at different pressures in the range $5 \div 100$ Pa. The background gas was either pure Ar or a mixture of Ar and H₂ (<3 vol%). The other process parameters were chosen upon optimization of the film quality in terms of reducing the formation of droplets.

The substrates for film deposition were monocrystalline $\langle 100 \rangle$ *p*-type silicon wafers, covered with a 120-nm-thick evaporated Al layer in the case of samples to be studied by Raman and SEM. The cleaning procedure consisted of rinsing the substrates with 2-propanol and drying with nitrogen. Target-to-substrate distance was set to 50 mm, and during deposition the substrate holder was rotated to widen uniformity over the deposition area.

All the samples were imaged by a Supra 40 Zeiss scanning electron microscope (SEM, accelerating voltage 2–4 kV) both in cross section and top-view, in order to characterize their morphology and thickness.

With the same instrument, energy-dispersive X-ray spectra (EDS) investigation was performed using an accelerating voltage of 5 kV, to excite $K\alpha$ electronic levels of O and Si, the signal being collected by a Si(Li) detector. We used $K\alpha$ of Silicon (1.74 keV) for system calibration, and every EDS analysis (250,000 counts) was repeated three times on different equivalent areas of the sample. We investigated the samples prepared at 100 Pa, in order to assess the degree of oxidation and to test the effect of using the mixture of Ar and H₂ (<3 vol%), instead of pure Ar, as deposition gas.

Amorphous/crystalline structure of the films was characterized by confocal Raman spectroscopy, with a Renishaw In-via micro-Raman system equipped with monochromator, notch filter, and charge-coupled detector.

Raman spectra were acquired upon excitation by a He–Cd laser (325 nm), or the second harmonic (532 nm) of an air-cooled Nd:YAG laser. The laser power for the 532 nm beam was lowered down to 0.3 mW (sample surface), in order to avoid laser-induced sample annealing. Spectra were typically recorded in the range 200–2,000 cm⁻¹ in the Stokes region and were calibrated against the 520.5 cm⁻¹ line of an internal silicon wafer reference. The signal to noise ratio was enhanced by repeated acquisitions.

Selected samples were analyzed by transmission electron microscopy (TEM) in order to reveal the presence, spatial dispersion, and dimension of nanocrystals, as well as the structure of the film. For the TEM investigation, the samples were prepared by scratching the film by means of a diamond tip, dispersing the fragments in few mL toluene and dripping the suspension on a commercial copper grid covered with a few nm thick carbon film on top of a carbon net.

Diffraction-contrast TEM imaging and electron diffraction analysis were carried out with a Jeol JEM 1011 instrument, equipped with a thermionic tungsten source, operated at 100 kV. High-resolution TEM (HR-TEM), energy-filtered TEM (EFTEM), and scanning TEM-high angle annular dark field (STEM-HAADF) analyses were performed with a Jeol JEM 2200FS instrument, equipped with a Schottky FEG W source, operated at 200 kV, and with a CEOS image aberration corrector and an in-column energy filter.

Results and discussion

Without undergoing any post-deposition thermal processes, all the samples were imaged by SEM and investigated by Raman spectroscopy, in order for their morphology and structure (amorphous/crystalline) to be characterized.

On some selected samples, EDS and TEM analyses were carried out, which allowed to examine, respectively, the film chemical composition and the presence, dimension, and spatial density of nanocrystalline phases in the film.

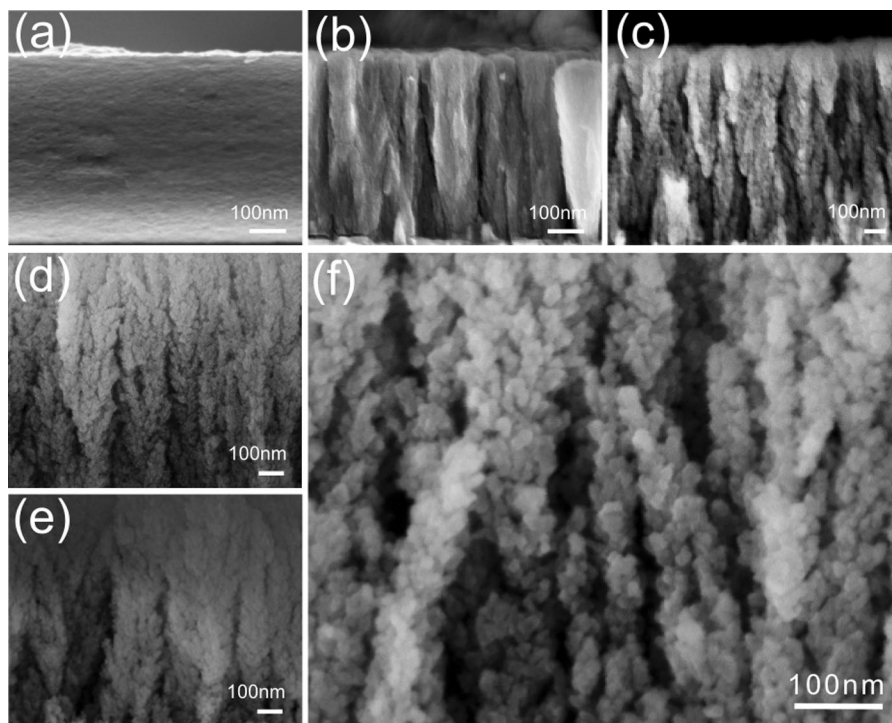


Fig. 1 Cross section SEM images of films grown at different pressures. With increasing deposition pressure, a transition in film morphology can be observed. **a** Compact structure deposited at 5 Pa Ar + H₂; **b** a columnar-dense film deposited at 40 Pa Ar + H₂; **c** columnar porous film deposited at 60 Pa

Ar + H₂; **d** columnar microporous algae-like film deposited at 100 Pa Ar + H₂ and **e** its analogous deposited at 100 Pa pure Ar showing no substantial difference in morphology. In **f** zoomed image of the film deposited at 100 Pa Ar + H₂

SEM images of the cross section of the film show that, starting from dense structures, grown at relatively low gas pressure (i.e., 5 Pa, Fig. 1a), the morphology of the film develops into an algae-like columnar hierarchical structure with increasing porosity upon increasing gas pressure (Fig. 1b–e). The influence of deposition gas pressure on the film nanoscale morphology is in full agreement with what observed for other materials, such as titanium oxide (Di Fonzo et al. 2009), and no significant differences in the evolution of film morphology are evidenced by comparing films produced in the same pressure of Ar or Ar + H₂ (Fig. 1d, e). In Fig. 1f, a zoomed cut of Fig. 1d allows to appreciate the granular structure of the hierarchical film grown at 100 Pa Ar + H₂.

From EDS investigation on samples deposited at 100 Pa (see Table 1), the use of a mixture of H₂ and Ar as deposition gas instead of pure Ar is proved to have a beneficial effect on reducing the oxygen content of the film, being amorphous Si passivation by H₂ very well

Table 1 Data from fitted EDS spectra for two films deposited with a background pressure of 100 Pa of pure Ar and Ar + H₂

Sample	Si (at.%)	O (at.%)	Impurities (C, N) (at.%)	O:Si ratio
Ar 100 Pa	34.8 (±0.1)	58.2 (±1.0)	6.9 (±1.0)	8:5
Ar + H ₂ 100 Pa	66.6 (±2.5)	28.5 (±0.3)	4.9 (±1.0)	2:5

The introduction of hydrogen in the gas mixture during deposition has the clear effect of reducing the oxygen content in the film through Si–H bond passivation. The oxygen to silicon ratio decreases by a factor 4 from pure Ar atmosphere (first row) to Ar + H₂ atmosphere (second row)

known in semiconductor processing (Honda et al. 2005; Pankove et al. 1984; Mott et al. 1975; Fuhs et al. 2006) (a reduction factor of about 4 in oxygen content is estimated with respect to the partially oxidized analogous Si layer deposited in pure Ar). Rather than obtaining an absolute value for the content of silicon,

this being unachievable when using a Si-based detector, or exactly assigning a value to the Si/O ratio in the two films, the EDS investigation was aimed at giving useful qualitative indications for improving fabrication, based on the variation in the Si/O ratio possibly induced by the mixture of H₂ in Ar. During the analysis, the Al layer has never been detected, thus excluding any contribution of the silicon substrate to the EDS signal.

Raman investigations reveal the presence of silicon nanocrystals embedded in an amorphous matrix in the samples grown at 100 Pa both in Ar and in Ar + H₂.

In Fig. 2a, the Raman spectra of samples produced at selected pressures from 5 to 100 Pa in Ar + H₂ are shown.

The spectra can be well fitted by four characteristic Gaussian bands, centered around 145, 330, 430, and 490 cm⁻¹, that are generally attributed, respectively, to the transverse acoustic (TA), longitudinal acoustic (LA), longitudinal optic (LO), and transverse optic (TO) modes of amorphous silicon (Li et al. 2011). Crystalline bulk silicon is known to have Raman spectrum denoted by a sharp peak at 520.5 cm⁻¹, related to the TO mode.

Only in the samples produced at 100 Pa, either in Ar or in Ar + H₂, does a peak appear on top of the band referred to amorphous silicon, in a position that varies, according to the chosen point on the sample, in the range between 514 and 517 cm⁻¹ and with a FWHM ranging between 12 and 14.5 cm⁻¹, as can be seen in Fig. 2b. This peak can be attributed to the TO mode of silicon crystals of nanometric size. The peak shift (3.5–6.5 cm⁻¹) and width broadening with respect to bulk crystalline silicon are agreed to be due to the quantum confinement effects via scattering of phonons away from the Brillouin zone center (relaxation of the $q = 0$ selection rule) (Richter et al. 1981; Duan et al. 2012).

No significant differences are detected in the spectral region under analysis for samples deposited either in pure Ar or in Ar + H₂ at the same pressure, as evidenced, e.g., by comparing the two spectra in Fig. 2b. The intensity of the nanocrystalline peak varies from spot to spot on the same sample, and it can be thus related to the local density of nanocrystallites under the investigation spot.

Several semi-empirical models have been proposed to relate the shift in Raman nanocrystalline peak to the dimension of the crystal itself (see Faraci et al. 2006;

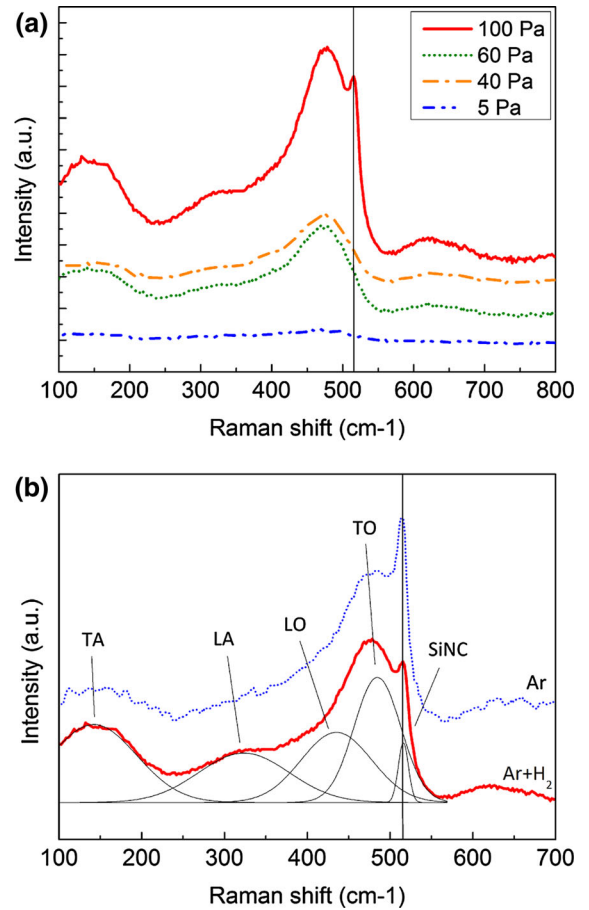


Fig. 2 a Raman spectra of samples deposited at different pressures in Ar + H₂ atmosphere. *Blue dash-dot-dotted, green dotted, and orange dash-dotted* (corresponding to samples deposited at 5, 40, and 60 Pa, respectively) show typical features of amorphous Si (four Gaussian bands at 142, 330, 435, and 485 cm⁻¹ attributed to TA, LA, LO, and TO modes). *Red solid curve* (sample deposited at 100 Pa) shows a peak appearing at 515 cm⁻¹, ascribable to nanocrystalline silicon (*bar* placed at 515 cm⁻¹ for easier reading). **b** *Red solid curve* Raman spectrum of a sample deposited at 100 Pa Ar + H₂, well fitted by the four components of amorphous Si and an additive peak centered at 515 cm⁻¹. *Dotted blue curve* Raman spectrum of a sample deposited at 100 Pa Ar, showing the same features as the one deposited in Ar + H₂ atmosphere. (Color figure online)

Richter et al. 1981). Using the formula proposed by He et al. (1994) to estimate the crystal diameter from the peak shift

$$d = 2\pi \left(\frac{B}{\Delta\omega} \right)^n,$$

where d is the crystal diameter, $\Delta\omega$ the peak shift from bulk position, $B = 2.0$ cm/nm (Li et al. 2011; He et al.

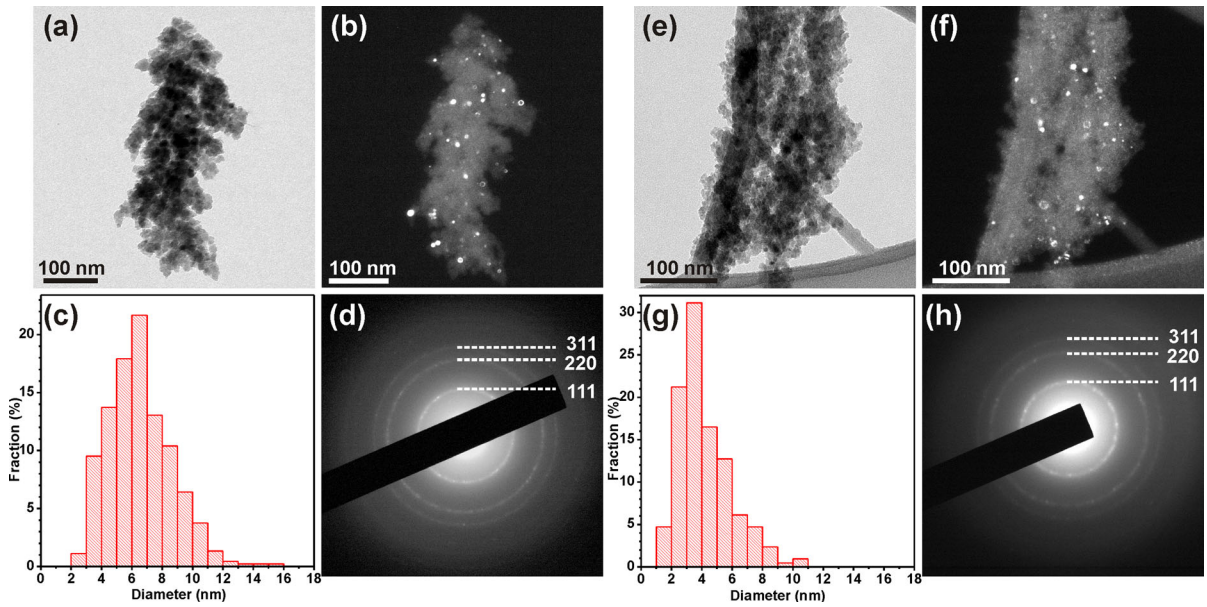


Fig. 3 **a–d** refer to fabrication in Ar, while **e–h** to fabrication in Ar + H₂. **a, e** BF-TEM images of fragments of the two samples and **b, f** corresponding DF-TEM images, obtained by selecting a region of the inner diffraction rings. **c, g** Histograms of the

particle size distribution in the two samples; the sample produced in Ar + H₂ shows smaller mean value. **d, h** ED patterns obtained by selecting the fragments in (**a, e**), respectively

1994) and $n = 0.5$ (He et al. 1994), a shift of $3.5\text{--}6.5\text{ cm}^{-1}$ gives a crystal size of $3.5\text{--}4.7\text{ nm}$ diameter.

No crystalline peak is traced for samples deposited at gas pressure lower than 100 Pa, thus denoting a threshold pressure for the nanocrystals to be synthesized.

TEM and HRTEM investigations confirm the presence of single-crystalline spherical nanoparticles, embedded in an amorphous matrix, on both the samples fabricated at 100 Pa in Ar + H₂ and in pure Ar as hereafter described.

Bright field TEM (BF-TEM) (Fig. 3a for Ar and 3e for Ar + H₂) confirms the hierarchical structure observed by SEM for the film fragments, composed by $\sim 10\text{ nm}$ -sized granules. Electron diffraction patterns acquired by selecting several fragments (Fig. 3d for Ar and 3h for Ar + H₂) show rings corresponding to randomly oriented crystalline silicon grains (cubic, space group $Fd\bar{3}m$, $a = 5.4309\text{ \AA}$, ICSD #652257).

Although only a weak diffraction contrast is appreciable in BF-TEM mode, dark-field (DF-TEM) images, obtained by selecting portions of the diffraction rings with the objective lens aperture (Figs. 3b, 4a, c for Ar and 3f, 4d, f for Ar + H₂), clearly show

that for both samples the material is formed by a matrix that includes several crystalline grains (appearing bright in DF-TEM due to the favorable diffraction condition), mainly spherical. From DF images, an average size of the crystallites can be determined as $6 (\pm 2)\text{ nm}$ for the sample produced in Ar and $4 (\pm 2)\text{ nm}$ for the sample produced in Ar + H₂, as summarized in the histograms shown in Fig. 3c for Ar and 3g for Ar + H₂ and in Table 2. The discrepancy with the size estimated from the Raman peak shift could be ascribed both to the simplified model adopted to take into account quantum confinement effects in Raman scattering from a spherical nanocrystal and to the possible presence of defects in nanocrystals introducing disorder and thus reducing the size of coherent-scattering domains.

HRTEM analyses on samples fabricated at 100 Pa in pure Ar and in Ar + H₂ confirm the presence of single-crystal Si particles, embedded in an amorphous porous matrix (Fig. 4b for Ar and 4e for Ar + H₂). Besides “bulk” nanocrystals, spherical particles of comparable size but with a more complex structure can also be found, as exhibited both by DF-TEM (bright rings or disk-ring systems, see Figs. 3b, 4a, c for Ar and 3f, 4d, f for Ar + H₂) and HRTEM analyses

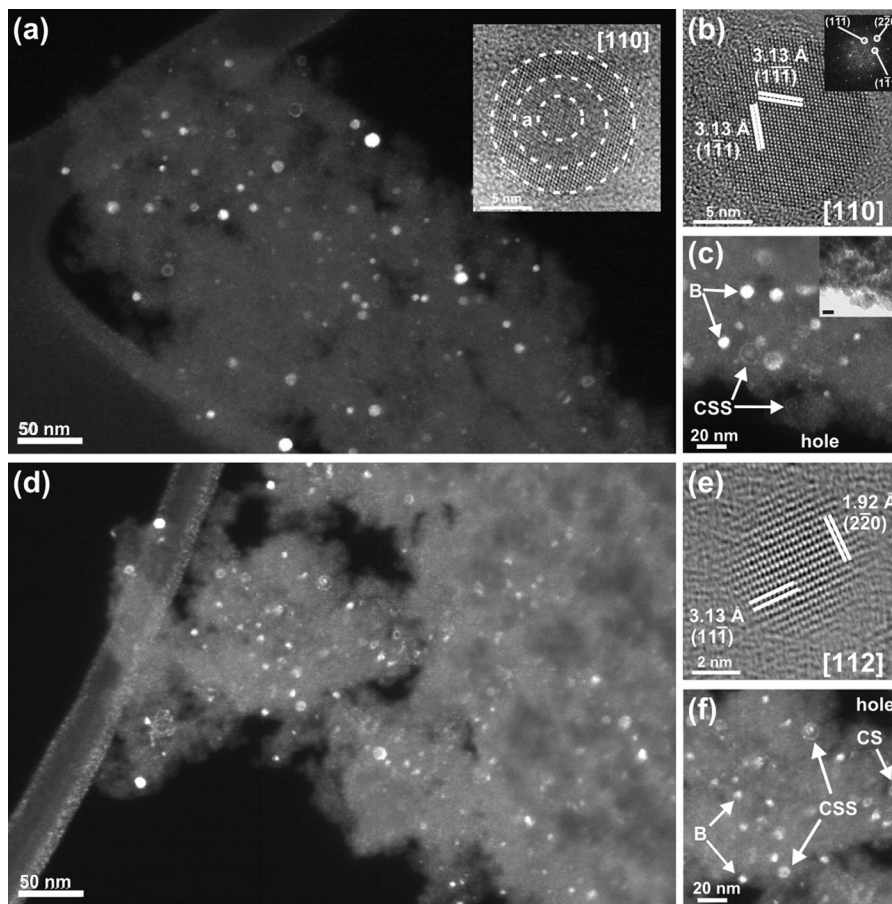


Fig. 4 For straightforward comparison, **a–c** refer to fabrication in 100 Pa Ar, while **d–f** in 100 Pa Ar + H₂. **a** DF-TEM image of a region of the sample made in Ar, showing bulk nanocrystals together with CS and CSS grains, all embedded in an amorphous matrix and **c** a zoomed view of the same, where CSS and bulk grains are highlighted. The *inset* in **c** shows the corresponding BF-TEM image. **b** HRTEM image of a bulk grain in the same sample, with the fast Fourier transform in the *inset* showing the

[110] pattern of single-crystal Si. (*inset* in **a**) HRTEM image of a core-shell-shell (CSS) crystal in the same sample, also showing [110] orientation. **d** DF-TEM image of a region of the sample made in Ar + H₂ showing bulk nanocrystals together with CS and CSS grains, all embedded in an amorphous matrix and **f** a zoomed view of the same, where CS, CSS, and bulk grains are highlighted. **e** HRTEM image of a bulk grain in the same sample

(*inset* in Fig. 4a). Upon further investigation, some of them turn out to have a unique CS structure, where the shell is crystalline and the core amorphous, and some of them show a thin amorphous shell in between the single-crystalline core and the outer crystalline shell (core-shell-shell, CSS). Such structures, which have never been obtained for silicon in a direct single-step process, have been synthesized in this work through the PLD process.

The regions appearing dark within the CS and CSS features in DF-TEM images are not hollow, or filled with gas, but characterized by a similar

composition and density as the bright regions. This is clearly demonstrated by comparing HRTEM images and EFTEM maps of the CSS grains (Fig. 5a and b in Ar): all the three regions (core, inner shell, outer shell) in the HRTEM image show the same composition, i.e., silicon, in the EFTEM maps.

HRTEM observations for samples deposited at 60 Pa (not shown) confirm that crystalline nanoparticles or CS/CSS structures are absent when lower deposition pressures are employed, in agreement with Raman spectra discussed above.

Table 2 Data of crystal grain dimension, volumetric fraction, volumetric density, and bulk/non-bulk fraction in samples produced at 100 Pa Ar or Ar + H₂, based on the analyses of DF-TEM images and EFTEM thickness maps

	Ar	Ar + H ₂
Average crystal size d_{average}	6 nm ± 2 nm	4 nm ± 2 nm
Number of grains in the fragment n_{tot}	341	212
Volume of the fragment V_{fragment}	2,800,000 nm ³	2,100,000 nm ³
Volume fraction occupied by grains = $\frac{V_{\text{tot grains}}}{V_{\text{fragment}}}$	2 %	0.4 %
Volumetric numerical density = $\frac{n_{\text{tot}}}{V_{\text{fragment}}}$	1.2×10^5 grains/ μm^3	1.0×10^5 grains/ μm^3
Fraction of the CS–CSS Grains $\frac{n_{\text{CS–CSS}}}{n_{\text{tot}}}$	10 %	4 %
Fraction of the Bulk Grains $\frac{n_{\text{bulk}}}{n_{\text{tot}}}$	90 %	96%

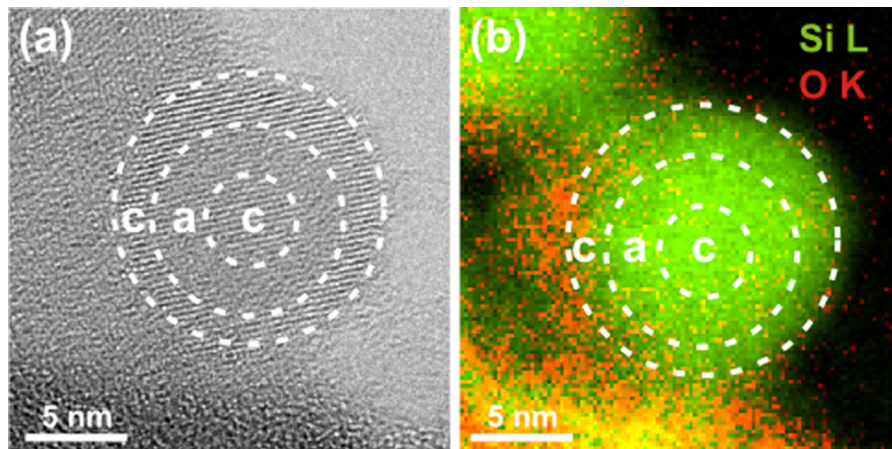


Fig. 5 **a** HRTEM image and **b** corresponding composition of EFTEM elemental maps of O (red) and Si (green) of a CSS grain in the film grown in Ar: all the three regions (core, inner shell,

outer shell) in the HRTEM image show the same composition, i.e., mainly silicon. (Color figure online)

Besides this observations, EFTEM elemental mapping indicates that the amorphous matrix surrounding the single-crystal grains is oxidized, as imaged in color in Fig. 5b, confirming the results obtained by EDS analysis (see above). An oxidized layer is visible (red) on the surface of Si grains (green). The sample here imaged was produced in pure Ar (no H₂) at high pressure. This sets favorable conditions for oxidation, because of two main reasons: the surface exposed to oxidation being high due to the high porosity, and the lack of any passivation effect induced by H₂ during deposition, as proven from EDS data. Therefore, the content of oxygen in this film can be considered as an upper limit for the whole bunch of samples, since EDS

measurements indicate a reduced content of oxygen in films deposited in the mixture of Ar and H₂ (H₂ <3 vol%).

Based on the DF-TEM images, an average volume density was evaluated for the grains for both samples prepared in Ar and Ar + H₂, and results are summarized in Table 2. For this purpose, images were acquired covering half (180°) of the innermost diffraction rings in the diffraction pattern and counting the grains in each corresponding image. However, in this way, the number of grains visualized and analyzed has to be considered as a lower limit, as some of the grains might not have been in a favorable diffraction condition. The thickness of each corresponding film

fragment was evaluated by acquiring EFTEM thickness maps, based on the inelastic scattering of the electrons (log-ratio method Egerton 2011). Based on the results of this analysis, summarized in Table 2, we are able to estimate a percentage of the analyzed volume occupied by crystalline QDs of about 2 % for the sample made in Ar and 0.4 % for Ar + H₂ and a volumetric density of the order of 1.2×10^5 grains/ μm^3 for the sample made in Ar and 1.0×10^5 for Ar + H₂. The volume of CS and CSS structures has been counted as “full,” i.e., as if all of the grains were bulk-type, to estimate the volumetric density.

Table 2 allows for direct comparison between the two samples, with Ar + H₂ showing, on average, smaller grains and a less pronounced occurrence of CS–CSS structures.

In Table 3, a careful analysis based on the same method was carried out on number, dimension, and volume fraction of the grains in sample fabricated in Ar + H₂, the results of which are detailed for bulk and “non-bulk” (CS–CSS) grain type.

For a proper evaluation of all of these numbers, one has to consider that the value for the volume of the fragment does not count for its porosity. An estimate of density has been done by knowing weight and thickness of the film, and values of 0.36 g/cm³ at 100 Pa (corresponding to a porosity of about 85 %), 0.92 g/cm³ at 60 Pa and 1.66 g/cm³ at 40 Pa were found (bulk silicon density being 2.33 g/cm³), independently of the processing gas.

The so assessed synthesis of crystalline Si nanoparticles at room substrate temperature may find explanation if one considers that in PLD strong out-of-equilibrium conditions can be established during the plume expansion prior to deposition on the substrate. The laser ablation plume expansion, in fact, can be strongly spatially confined by the presence of a background gas (Geohegan et al. 1998; Merkulov et al. 1994; Amoroso et al. 2006), with a traveling shock wave front, which slows down until it reaches the so-called stopping distance and is characterized by high pressure, temperature, and density gradients at the shock front, if ablation occurs in a relatively high background pressure, resulting in strong out-of-equilibrium conditions (Arnold et al. 1999; Leboeuf et al. 2009; Lowndes et al. 1996). This situation is favorable for cluster nucleation and we suppose that, if a threshold background deposition pressure is overcome, it can induce proper energetic conditions at the shock wave

Table 3 Detailed data of grain dimension and density for bulk and non-bulk (CS–CSS) grains in sample produced at 100 Pa Ar + H₂

Bulk grains			
Average crystal size	d_{average}		4.0 nm \pm 1.5 nm
Number of full grains in the fragment	n_{bulk}		203
Volume fraction occupied by grains	$\frac{V_{\text{bulk grains}}}{V_{\text{fragment}}}$		3.2×10^{-3}
Volumetric numerical density	$\frac{n_{\text{bulk grains}}}{V_{\text{fragment}}}$		9.7×10^4 grains/ μm^3
Fraction of the full grains	$\frac{n_{\text{bulk}}}{n_{\text{tot}}}$		96 %
CS–CSS grains			
Average crystal size	d_{average}		8.0 nm \pm 1.5 nm
Number of CS–CSS grains in the fragment	$n_{\text{CS–CSS}}$		9
Volume fraction occupied by grains	$\frac{V_{\text{CS–CSS grains}}}{V_{\text{fragment}}}$		1.1×10^{-3}
Volumetric numerical density	$\frac{n_{\text{CS–CSS}}}{V_{\text{fragment}}}$		4.3×10^3 grains/ μm^3
Fraction of the CS–CSS grains	$\frac{n_{\text{CS–CSS}}}{n_{\text{tot}}}$		4 %
All grains			
Average crystal size	d_{average}		4.2 nm \pm 1.7 nm
Number of grains in the fragment	$n_{\text{all grains}}$		212
Volume fraction occupied by grains	$\frac{V_{\text{all grains}}}{V_{\text{fragment}}}$		3.9×10^{-3}
Volume fraction occupied by grains	$\frac{n_{\text{all grains}}}{V_{\text{fragment}}}$		1.0×10^5 grains/ μm^3

front leading to condensation of crystalline nanoparticles in the region of the traveling shock wave front, which can then diffuse in the background gas decreasing their kinetic energy. This process leads to low energy deposition thus producing a cluster-assembled material in which preformed Si QDs maintain, at least partially, their structure and properties.

CS crystalline-amorphous nanoparticles and hollow nanospheres have been recently reported by Sturm and coworkers in the synthesis of Sm–Fe(Ta)–N structures by PLD in a 1 atm nitrogen pressure, together with a detailed and systematic analysis of the sequence of steps occurring during the ablation–deposition process and of the growth mechanisms of such nanostructures (Sturm et al. 2010). They involve the formation of nanocrystals and CS or void-shell structures from solidification of a multi-component system, with the main determining parameter for the

formation of either CS or filled nanocrystals being the amount of dissolved gas in the initial molten droplet. The proposed explanation cannot be directly extended to our case, due to the different material structures and experimental conditions; however, we cannot exclude that a similar mechanism may occur involving solidification of silicon aggregates in the presence of dissolved gas atoms (argon).

Alternatively, we can infer that in our case the presence of strong temperature gradients may be responsible for the observed peculiar CS nanostructures. A possible formation mechanism may be related to a crystallization process starting at the surface of Si clusters formed in the ablation plume, followed, in particular conditions, by a rapid local thermal annealing leading to an amorphous core. Considering that molten silicon releases latent heat at solidification, the observed unique structure can be the effect of a “recalescence” process, that is, an increase in temperature that appears while cooling through a range of temperatures in which change in structure occurs, likely caused by local heat released at solidification and mainly governed by laser energy density. This amorphization process, already observed in the case of solidification of silicon thin films (Sameshima and Usui 1991a, b) after melting by laser irradiation, has been supposed to be mainly initiated by laser energy density, when its value is just above the melting threshold, and it seems to be the most plausible process to be invoked in the formation of our CS nanostructures. As suggested in the work of Sameshima and Usui (1991a), it can be interpreted as cooling of the molten silicon layers to an isothermal supercooled state and followed by fast solidification.

Conclusions

In summary, we have described a single-step physical vapour deposition method for the fabrication at room temperature of silicon nanocrystals and more complex silicon amorphous-crystalline CS nanostructures embedded in a porous amorphous matrix. Nanostructured silicon films with different porosities have been thus grown by PLD in argon or in a mixture of argon and few percents of hydrogen as buffer gas. Without any further post-deposition steps, samples deposited at relatively high pressure (100 Pa) repeatedly exhibit the presence of Si nanocrystals as revealed by Raman investigation and

confirmed by TEM analysis. For all the samples, with or without nanocrystals, the porosity of the film has been controlled by suitable deposition parameters and features a wide range of structures, from very compact to columnar algae-like shaped. In situ oxidation of the film has been effectively reduced by the presence of few percentage of hydrogen gas into the pure argon gas. Notably, the fabrication of silicon nanocrystals via PLD represents an excellent alternative to obtain these structures at room temperature without any further high-temperature steps and offers the possibility of tailoring the properties of the crystals and of the amorphous matrix.

The proposed synthesis approach can be exploited in the near future to obtain Si nanocrystals in different matrices (e.g., silicon oxide, carbide, or nitride) and therefore realize a system of Si QDs embedded in a compact host matrix, possibly allowing for efficient charge transport through the QD network. Moreover, these novel CS nanostructures, where the Si crystalline shell could in principle work as a stable mechanical support and efficient electrical conducting pathway, while the amorphous core should lead to an improvement of the material optical characteristics (low-grade amorphous silicon with long range disorder in its atomic structure behaves like a direct-bandgap semiconductor with two-orders higher optical absorption coefficient as compared with its crystalline counterpart), may represent a novel approach to address the issues associated with silicon nanostructures and thin films for different applications.

Acknowledgments The authors gratefully acknowledge Mirko Prato, Valeria Russo, and Tushar Salve for useful discussion.

References

- Amoruso S et al (2006) Propagation of LaMnO₃ laser ablation plume in oxygen gas. *Appl Surf Sci* 252(13):4712–4716. doi:10.1016/j.apsusc.2005.07.107
- Arnold N, Gruber J, Heitz J (1999) Spherical expansion of the vapor plume into ambient gas: an analytical model. *Appl. Phys. A* 69:87–93
- Borsella E et al (2010) Biomedical and sensor applications of silicon nanoparticles. In: Pavesi L, Turan R (eds) *Silicon nanocrystals*. Wiley-VCH Verlag GmbH & Co. KGaA, Weinheim, pp 507–536
- Bruno P et al (2011) Pulsed laser deposition of silicon nanostructures. *MRS Proc* 1322:mrss11-1322-b05-34. http://journals.cambridge.org/abstract_S1946427411012929. Accessed 17 Dec 2013

- Casari CS, Bassi AL (2012) Pulsed laser deposition of nanostructured oxides: from clusters to functional films. In: Arkin WT (ed) *Advances in laser and optics research*. Nova Science Publishers Inc., New York, pp 65–100
- Cheng Q et al (2010) Si quantum dots embedded in an amorphous SiC matrix: nanophase control by non-equilibrium plasma hydrogenation. *Nanoscale* 2(4):594–600. <http://www.ncbi.nlm.nih.gov/pubmed/20644764>. Accessed 3 April 2013
- Cheng X et al (2012) One-pot synthesis of colloidal silicon quantum dots and surface functionalization via thiol-ene click chemistry. *Chem Commun (Camb)* 48(97):11874–11876. <http://www.ncbi.nlm.nih.gov/pubmed/23125971>. Accessed 7 April 2013
- Conibeer G (2010) Applications of Si nanocrystals in photovoltaic solar cells. In: Pavesi L, Turan R (eds) *Silicon nanocrystals*. Wiley-VCH Verlag GmbH & Co. KGaA, Weinheim, pp 555–582
- Conibeer G et al (2006) Silicon nanostructures for third generation photovoltaic solar cells. *Thin Solid Films* 511–512:654–662. <http://linkinghub.elsevier.com/retrieve/pii/S0040609005024703>. Accessed 4 April 2012
- Conibeer G et al (2009) Progress on hot carrier cells. *Solar Energy Mater Sol Cells* 93(6–7):713–719. <http://linkinghub.elsevier.com/retrieve/pii/S0927024808002882>. Accessed 23 March 2013
- Conibeer G et al (2010) Modelling of hot carrier solar cell absorbers. *Solar Energy Mater Sol Cells* 94(9):1516–1521. <http://linkinghub.elsevier.com/retrieve/pii/S0927024810000334>. Accessed 27 March 2013
- Dellasega D et al (2012) Nanostructured and amorphous-like tungsten films grown by pulsed laser deposition. *J Appl Phys* 112(8):084328. <http://link.aip.org/link/JAPIAU/v112/i8/p084328/s1&Agg=doi>. Accessed 6 May 2013
- Di Fonzo F et al (2009) Hierarchically organized nanostructured TiO₂ for photocatalysis applications. *Nanotechnology* 20(1):015604. <http://www.ncbi.nlm.nih.gov/pubmed/19417258>. Accessed 8 March 2013
- Duan Y, Kong JF, Shen WZ (2012) Raman investigation of silicon nanocrystals: quantum confinement and laser-induced thermal effects. *J Raman Spectrosc* 43(6):756–760. doi:10.1002/jrs.3094
- Egerton RF (2011) *Electron energy-loss spectroscopy in the electron microscope*, 3rd edn. Springer, New York
- Faraci G et al (2006) Modified Raman confinement model for Si nanocrystals. *Phys Rev B* 73(3):1–4. doi:10.1103/PhysRevB.73.033307
- Fuhs W, Korte L, Schmidt M (2006) Heterojunctions of hydrogenated amorphous silicon and monocrystalline silicon. *J Optoelectron Adv Mater* 8(6):1989–1995. <http://www.hmi.helmholtz.de/media/media/spezial/people/korte/publications/6fuhs.pdf>. Accessed 17 Dec 2013
- Fusi M et al (2009) Titanium oxide nanostructured films by reactive pulsed laser deposition. *Appl Surf Sci* 255(10):5334–5337. <http://linkinghub.elsevier.com/retrieve/pii/S0169433208017182>. Accessed 14 March 2013
- Geohegan DB et al (1998) Time-resolved imaging of gas phase nanoparticle synthesis by laser ablation. *Appl Phys Lett* 72(23):2987. <http://link.aip.org/link/APPLAB/v72/i23/p2987/s1&Agg=doi>. Accessed 27 March 2013
- Hartel AM et al (2011) Formation of size-controlled silicon nanocrystals in plasma enhanced chemical vapor deposition grown SiO_xN_y/SiO₂ superlattices. *Thin Solid Films* 520(1):121–125. <http://linkinghub.elsevier.com/retrieve/pii/S0040609011013617>. Accessed 30 April 2012
- He Y et al (1994) The structure and properties of nanosize crystalline silicon films. *J Appl Phys* 75(2):797. <http://link.aip.org/link/JAPIAU/v75/i2/p797/s1&Agg=doi>. Accessed 26 Nov 2012
- Honda S et al (2005) Effect of hydrogen passivation on polycrystalline silicon thin films. *Thin Solid Films* 487(1–2):152–156. <http://linkinghub.elsevier.com/retrieve/pii/S0040609005000854>. Accessed 15 March 2013
- Kim H et al (2010) A critical size of silicon nano-anodes for lithium rechargeable batteries. *Angew Chem Int Ed* 49(12):2146–2149
- König D et al (2010) Hot carrier solar cells: principles, materials and design. *Phys E* 42(10):2862–2866. <http://linkinghub.elsevier.com/retrieve/pii/S138694770900650X>. Accessed 23 March 2013
- Leboeuf JN et al (2009) Modeling of dynamical processes in laser ablation. *Appl Surf Sci* 96:14–23
- Li Z et al (2011) Raman characterization of the structural evolution in amorphous and partially nanocrystalline hydrogenated silicon thin films prepared by PECVD. *J Raman Spectrosc* 42(3):415–421. doi:10.1002/jrs.2711
- Lowndes DH et al (1996) Synthesis of novel thin-film materials by pulsed laser deposition. *Science* 273(5277):898–903
- Luque A, Martí A, Nozik AJ (2007) Solar cells based on quantum dots: multiple exciton generation and intermediate bands. *MRS Bull* 32:236–241
- Mangolini L, Kortshagen U (2007) Plasma-assisted synthesis of silicon nanocrystal inks. *Adv Mater* 19(18):2513–2519. doi:10.1002/adma.200700595
- Mangolini L, Thimsen E, Kortshagen U (2005) High-yield plasma synthesis of luminescent silicon nanocrystals. *Nano Lett* 5(4):655–659. <http://www.ncbi.nlm.nih.gov/pubmed/15826104>. Accessed 27 March 2013
- Marine W et al (2000) Strategy of nanocluster and nanostructure synthesis by conventional pulsed laser ablation. *Appl Surf Sci* 154–155:345–352. <http://linkinghub.elsevier.com/retrieve/pii/S016943329900450X>. Accessed 27 March 2013
- Merkulov VI, Lowndes DH, Jellison GE (1994) Synthesis and characterization of pulsed-laser deposited amorphous carbon films. In: Chrisey DB, Hubler G (eds) *Pulsed laser deposition of thin films*. Wiley & Sons, New York, p 115
- Mott NF, Davis EA, Street RA (1975) States in the gap and recombination in amorphous semiconductors. *Philos Mag* 32(5):961–996. doi:10.1080/14786437508221667
- Muralidhar R, Sadd MA, White JBE (2009) Silicon nanocrystal nonvolatile memories. In: Koshida N (ed) *Device applications of silicon nanocrystals and nanostructures*. Springer, Boston, pp 223–249. <http://www.springerlink.com/index/10.1007/978-0-387-78689-6>. Accessed 6 Aug 2013
- Nozik A (2002) Quantum dot solar cells. *Phys E* 14(1–2):115–120. <http://linkinghub.elsevier.com/retrieve/pii/S1386947702003740>. Accessed 27 March 2013
- Pankove JI, Wance RO, Berkeyheiser JE (1984) Neutralization of acceptors in silicon by atomic hydrogen. *Appl Phys Lett*

- 45(10):1100. <http://link.aip.org/link/?APPLAB/45/1100/1>. Accessed 15 March 2013
- Park S et al (2008) Study of silicon quantum dot p-n or p-i-n junction devices on c-Si substrate. In: 2008 conference on optoelectronic and microelectronic materials and devices, pp 316–319. <http://ieeexplore.ieee.org/lpdocs/epic03/wrapper.htm?arnumber=4802155>. Accessed 27 March 2013
- Richter H, Wang ZP, Ley L (1981) The one phonon Raman spectrum in microcrystalline silicon. *Solid State Commun* 39(5):625–629. doi:10.1016/0038-1098(81)90337-9
- Sameshima T, Usui S (1991a) Mechanism of pulsed laser-induced amorphization of silicon films. *Appl Phys Lett* 59(21):2724. <http://link.aip.org/link/APPLAB/v59/i21/p2724/s1&Agg=doi>. Accessed 17 May 2013
- Sameshima T, Usui S (1991b) Pulsed laser-induced amorphization of silicon films. *J Appl Phys* 70(3):1281. <http://link.aip.org/link/JAPIAU/v70/i3/p1281/s1&Agg=doi>. Accessed 17 May 2013
- Sturm S et al (2010) Formation of core-shell and hollow nanoparticles through the nanoscale melt-solidification effect in the Sm-Fe(Ta)-N system. *Nanotechnology* 21(48):485603. <http://www.ncbi.nlm.nih.gov/pubmed/21063053>. Accessed 7 May 2013
- Suzuki T et al (2012) Thermal conductivity of size-controlled bulk silicon nanocrystals using self-limiting oxidation and HF etching. *Appl Phys Express* 5(8):081302. <http://apex.jsap.jp/link?APEX/5/081302/>. Accessed 27 March 2013
- Tsakalacos L (2008) Nanostructures for photovoltaics. *Mater Sci Eng R* 62(6):175–189. <http://linkinghub.elsevier.com/retrieve/pii/S0927796X08000570>. Accessed 25 June 2011
- Umezu I et al (2007) Formation of nanoscale fine-structured silicon by pulsed laser ablation in hydrogen background gas. *Phys Rev B* 76(4):045328. doi:10.1103/PhysRevB.76.045328
- Umezu I, Nakayama Y, Sugimura A (2010) Formation of core-shell structured silicon nanoparticles during pulsed laser ablation. *J Appl Phys* 107(9):094318. <http://link.aip.org/link/?JAPIAU/107/094318/1>. Accessed 3 April 2013
- Wood RF et al (1998) Dynamics of plume propagation, splitting, and nanoparticle formation during pulsed-laser ablation. *Appl Surf Sci* 127–129:151–158. <http://linkinghub.elsevier.com/retrieve/pii/S0169433297006259>. Accessed 27 March 2013
- Wu YC, Wang LW, Lai CH (2008) (001) FePt nanoparticles with ultrahigh density of 10¹⁴ dots/in. 2 on amorphous SiO₂ substrates. *Appl Phys Lett* 93(24):242501. <http://link.aip.org/link/APPLAB/v93/i24/p242501/s1&Agg=doi>. Accessed 7 May 2013
- Yuan CL (2010) Room-temperature coercivity of Ni/NiO core/shell nanoparticles fabricated by pulsed laser deposition. *J Phys Chem C* 114(5):2124–2126. doi:10.1021/jp911015b